Glaucoma

DAMPs Drive Fibroinflammatory Changes in the Glaucomatous ONH

Emma K. Geiduschek, Emma K. Bricco, and Colleen M. McDowell

University of Wisconsin–Madison, Madison, Wisconsin, United States

PURPOSE. The optic nerve head (ONH) is well known to be the initial site of glaucomatous damage; however, the molecular mechanisms initiating this pathology are not fully understood. To further understand the initiating factors in glaucomatous damage we utilized a novel mouse model of glaucoma, B6.EDA$^{+/+}$ mice, which constitutively express fibronectin containing the extra domain A (FN+EDA). FN+EDA is a known damage-associated molecular pattern (DAMP) that activates Toll-like receptor 4 and elicits a fibro-inflammatory response.

METHODS. Eyes from B6.EDA$^{+/+}$ and C57BL/6J mice were evaluated for retinal ganglion cell (RGC) death, retinal nerve fiber layer (RNFL) thickness, and optic nerve (ON) damage at 12 months and 22 months of age. ONH sections were isolated using laser capture microdissection for subsequent RNA-sequencing and Gene Set Enrichment Analysis (GSEA). GSEA results were confirmed using immunohistochemical (IHC) staining.

RESULTS. B6.EDA$^{+/+}$ mice exhibit significantly higher intraocular pressure, loss of RGCs, thinning of the RNFL, and progressive levels of ON damage at 12 months and 22 months of age compared to C57BL/6J controls. Protein expression of DAMPs FN+EDA and biglycan was significantly increased in B6.EDA$^{+/+}$ mice compared to C57BL/6J controls. GSEA analysis identified significantly up- and downregulated gene groupings at both 12 months and 22 months of age, and IHC staining at 12 and 18 months of age demonstrated significant increases of IFNα, IFNβ, and pSTAT1 expression in B6.EDA$^{+/+}$ mice compared to C57BL/6J controls.

CONCLUSIONS. Our study characterizes glaucomatous changes to the retina, ON, and ONH over the course of 2 years and identifies novel molecular pathways associated with these pathophysiological changes. These data illustrate the effects of FN+EDA on the fibro-inflammatory response in the aging ONH in a novel mouse model of glaucoma.

Keywords: glaucoma, FN+EDA, optic nerve head, interferons, STAT1

Glaucoma is characterized by the loss of retinal ganglion cells (RGCs) and subsequent optic nerve head (ONH) damage resulting in a progressive loss of vision over time.[1–3] The primary site of RGC axonal damage occurs at the layer of the lamina cribrosa (LC) in the ONH which consists of a fenestrated stack of extracellular matrix (ECM) proteins that provide both physical support for the exiting RGC axons, as well as scaffolding for nutrient transport and vasculature. During disease progression, the ONH undergoes drastic remodeling. Disruption of the ECM in the LC region causes increased fibrosis, thickening of the connective tissue around the optic nerve (ON) fibers, elastosis, and thickening of the basement membranes, resulting in eventual mechanical failure adversely affecting the capacity of the LC to support the exiting RGC axons.[4–6] Although the mouse does not have a true LC, it has a glial lamina that has been shown to harbor similar glaucomatous changes during disease progression.[7,8]

Previous literature has heavily implicated both profibrotic and pro-inflammatory signaling cascades in the progression and exacerbation of glaucomatous damage.[4–6,9–17] One predominant hypothesis indicates that chronic exposure to mechanical stress and strain from elevated intraocular pressure (IOP), loss of nutrients, and hypoxic microenvironments produce a chronic level of inflammation through the innate immune system.[9–14] The role of innate immune system activation and subsequent glaucomatous pathology has been extensively reviewed,[9,18–20] often with a focus on the role of microglia as the resident macrophages of the central nervous system (CNS) immune responses. In homeostatic environments, microglia constantly monitor their local microenvironments and primarily clear debris and dead cells.[21] Upon activation from damage, or in disease states, microglia undergo drastic morphological changes from ramified surveyors to an ameboid shape and migrate to the cite of damage within a matter of minutes.[22–26] Microgliosis has been implicated in other CNS diseases such as Alzheimer's and Parkinson's disease, as well as glaucoma.[27] Activated microglia induce activation of astrocytes, which subsequently produce pro-inflammatory cytokines and chemokines that are able to initiate innate immune system signaling through Toll-like receptors (TLRs).[28,29]

Notably, Toll-like receptor 4 gene (*Tlr4*) polymorphisms have also been associated with an enhanced risk of glau-

Investigative Ophthalmology & Visual Science

coma in populations of different racial backgrounds, including Japanese and Mexican populations.[30–32] TLR4 was first discovered as the receptor for lipopolysaccharide,[33] but it is also activated by endogenous ligands referred to as damage-associated molecular patterns (DAMPs). DAMPs are produced in vivo from injury, cell damage, oxidative stress, or ECM accumulation.[34,35] TLR4 is known to be expressed in mouse and human RGC axons, ONH astrocytes, and ONH microglia,[7,36–38] indicating that it is a global activator of the innate immune system within the ONH. TLR4 pathway–related genes, downstream ECM genes, and TLR4-activating DAMPs, such as tenascin-C, heat shock proteins, and, importantly, the extra domain A (EDA) isoform of fibronectin (FN+EDA), are differentially expressed in the human ONH and retina in glaucoma.[39–42]

FN, a high-molecular-weight, multidomain glycoprotein, has previously been shown to be significantly increased in the glaucomatous trabecular meshwork (TM), aqueous humor (AH), and LC region of the ONH.[42–46] There are two types of FN found in vertebrates: cellular FN (cFN) and plasma FN (pFN).[47] Splice variants of cFN contain combinations of the EDA domain, extra domain B (EDB), and type III homologies. pFN does not contain the EDA or EDB domains.[47] FN+EDA expression is high during embryonic development but lowers to near-negligible expression levels in adult tissue.[48] However, during disease states or inflammatory responses, the expression of FN+EDA is upregulated.[49–52] Importantly, FN+EDA is increased in the glaucomatous human TM and ONH[42,53] and acts as a potent activator of TLR4 in TM cells[44,54] and ONH LC cells.[42]

Recently, we have shown that TGFβ2-induced ocular hypertension is dependent on both TLR4 and FN+EDA expression.[7,54] In addition, constitutive expression of FN+EDA is sufficient to induce ocular hypertension and modest glaucomatous damage in the retina and ON.[7,54] In this model, B6.EDA$^{+/+}$ mice constitutively express FN+EDA. These mice exhibit TLR4-dependent increased IOP starting from 14 weeks of age.[7,54] At 1 year of age, these mice have significant reductions in RGCs and increased levels of ON damage.[7] Interestingly, these mice show elevated levels of the microglia marker Iba1, as well as increased *Tlr4* mRNA in microglia compared to age-matched controls at 9 months of age, prior to any ONH or ON damage.[7] Here, we tested the progressive retinal and ONH damage in this novel mouse model in an aged state, in addition to elucidating transcriptome variations responsible for glaucomatous changes. We predict that aging leads to progressive glaucomatous damage driven by fibro-inflammatory signaling.

METHODS

Animals

The generation of B6.EDA$^{+/+}$ mice has been described previously,[49] and they constitutively express only FN containing the EDA domain. C57BL/6J mice were purchased from the The Jackson Laboratory (Bar Harbor, ME, USA) and aged at the University of Wisconsin–Madison. All animals were housed in the University of Wisconsin–Madison vivarium with a normal 12-hour light/dark cycle, and they were fed a 4% fat diet (Teklad; Envigo, Indianapolis, IN, USA) with food and water available ad libitum. All experiments conducted in compliance with the ARVO Statement for the Use of Animals in Ophthalmic and Vision Research.

For quantification of RGC loss and preparation for laser capture microdissection (LCM) of the ONH, mice were euth-

anized by CO_2 inhalation, and their eyes were nucleated. One eye was frozen on dry ice in optimum cutting temperature (OCT) compound (#4583; Sakura Finetek, CA, Torrance, USA) for subsequent LCM and RNA-sequencing (RNA-seq). The other eye was prepared for retinal flatmount analysis (see below). An additional group of animals was used for immunohistochemical analyses.

For the LCM, retina flatmount, and retinal nerve fiber layer (RNFL) thickness measurements, we used one eye per mouse for analysis. Both eyes were used for the ON paraphenylene-diamine (PPD) stain analysis and IOP measurements. We and others have previously analyzed both ONs from an animal and accounted for them as a single "*n*" based on the fact that it is well known that individual eyes can respond differently to chronic IOP changes.[7,55,56] Also, it is well known that IOP is not exactly the same between both eyes, and eyes are frequently used as the "*n*" in transgenic and chronic models of glaucoma.[7,55,56] For immunohistochemical (IHC) analysis, both eyes from each mouse were processed, but not all eyes were used in every analysis due to the limited number of sections obtained from each ONH. We used a minimum of eyes from three individual mice in each staining.

IOP Measurements

IOP was measured with a rebound tonometer as previously described at 12 months and 22 months of age.[7] IOP was measured in isoflurane anesthetized mice with the iCare TONOLAB tonometer (Icare Finland, Vantaa, Finland). Ten measurements per eye were averaged to represent one biological replicate at each time point ($n = 6$ to 9 mice/strain; 12–18 eyes). All measurements were made during the same 2-hour period of the lights-on phase in the morning.

Quantification of ON Damage

ON damage was assessed in sections of resin-embedded ONs stained with PPD. Retro-orbital ONs were embedded in plastic and stained with PPD, which stains the myelin sheaths and more darkly stains the axoplasm of sick or dying axons. Each section was ranked for damage by two individuals in a masked manner and then subsequently evaluated for consensus, as previously described ($n = 11$ to 15 ONs per strain per time point).[57,58] We and others have previously quantified ON damage using a semiquantitative ON grading scheme.[57,59–61] Here, we used a five-point grading scheme,[7,58] where a score of 1 represented no identifiable gliosis or axon swelling; a score of 2 represented 5% to 10% darkly stained axons, initial stages of gliosis, and little axon swelling; and a score of 3 represented 10% to 50% darkly stained axons, with the central part of the nerve involved and initial to mild gliosis. Scores of 4 and 5 representing severe damage were not seen in these experiments.

Quantification of RGC Loss and RNFL Thickness

Loss of RGCs was quantified in RNA-binding protein with multiple splicing (RBPMS)-labeled retinal flatmounts. Dissected retinas were immersed in 4% paraformaldehyde (PFA) in 100-nM PBS for 60 minutes at room temperature, then transferred to 30% sucrose in PBS. Retinas remained in 30% sucrose in PBS overnight at 4°C. The retinas were then frozen on dry ice for 10 minutes and allowed to thaw at benchtop for 15 minutes to perforate the cell membranes for efficient staining of intracellular proteins. The freeze/thaw
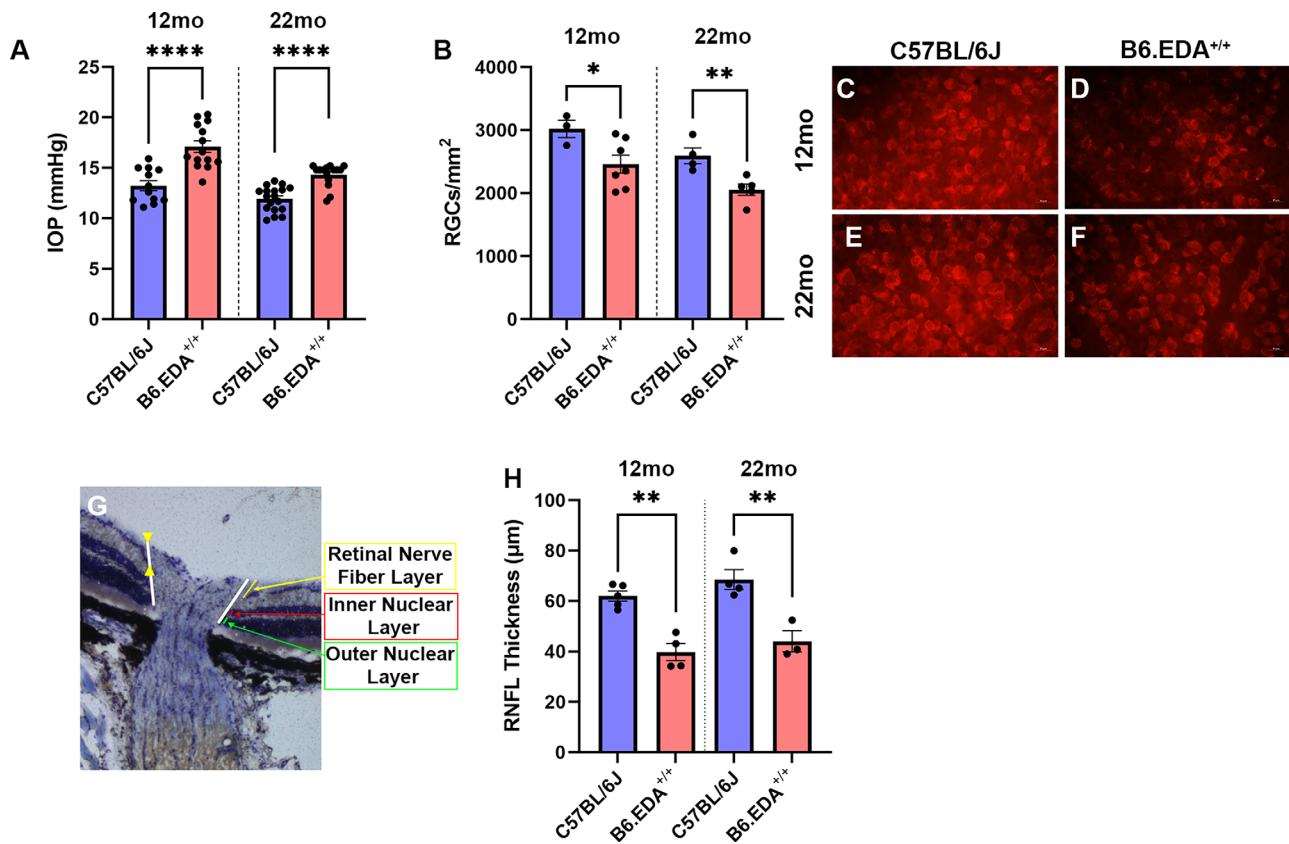
FIGURE 1. B6.EDA$^{+/+}$ mice exhibited glaucoma phenotypes at 12 months and 22 months of age. (**A**) IOP was significantly elevated in B6.EDA$^{+/+}$ mice at 12 months ($n = 12$ to 14 eyes/strain) and 22 months ($n = 16$ to 18 eyes/strain) compared to age-matched C57BL/6J controls. Significance was determined by Student's *t*-test at each time point. (**B**) B6.EDA$^{+/+}$ mice ($n = 3$ to 7 eyes/strain) showed an ∼20% loss of RGCs at both 12 months and 22 months of age compared to C57BL/6J controls, as quantified by RBPMS staining of retinal flatmounts. Significance was determined by Student's *t*-test at each time point. (**C–F**) Representative images of RBPMS staining at 12 months and 22 months for B6.EDA$^{+/+}$ mice and age-matched C57BL/6J controls. (**G**) The location for measurements of RNFL thickness was standardized by drawing a line from the bottom of the inner nuclear layer (*green line*) to the top of the outer nuclear layer (*red line*) and extended to the top of the RNFL (*yellow line*). Measurements were then taken for the RNFL thickness only (*yellow arrows*). (**H**) B6.EDA$^{+/+}$ mice exhibited significant thinning of the RNFL at both 12 months and 22 months of age compared to age-matched C57BL/6J controls ($n = 3$ to 5 eyes/strain). RNFL thickness was measured using ImageJ, and significance was determined by Student's *t*-test at each time point. *$P < 0.05$, **$P < 0.01$, ****$P < 0.0001$.

cycle was repeated two more times, and the retinas were then washed in 1× PBS three times for 1 hour each, as previously described.[62,63] After the last wash, the PBS was removed, and the retinas were blocked in 1× PBS containing 2% BSA and 0.1% Triton X-100 (Sigma-Aldrich, St. Louis, MO, USA) overnight. RGCs were labeled using anti-RBPMS antibody (#1830; PhosphoSolutions, Aurora, CO, USA) at 1:100 dilution overnight at 4°C. Primary antibody was washed off with 1× PBS three times for 1 hour each. Following the washes, the retinas were incubated with Cy 3 AffiniPure Donkey Anti-Rabbit IgG (H+L) (#711-165-152; Jackson ImmunoResearch, West Grove, PA, USA) at 1:200 dilution overnight at 4°C. Slides were then washed in 1× PBS three times for 1 hour each and mounted with VECTASHIELD Antifade Mounting Medium with DAPI (#H-1200-10; Vector Laboratories, Newark, CA, USA) and coverslipped. Retinal images were collected using a ZEISS Axio Imager.Z2 microscope (Carl Zeiss AS, Oslo, Norway). RBPMS-positive cells were counted in eight central and eight peripheral regions of the retina, modified from previously described methods.[7] Two quadrants (280 μm × 180 μm) located 0.7 mm (central region) and 1.4 mm (peripheral region) away from the ONH in each cardinal direction were selected. Cells were counted in a masked manner ($n = 3$ to 7 eyes per strain per time point). The RGC count was obtained for each retina by averaging the 16 fields and determining the average RGC count per square millimeter.

Thinning of the RNFL was quantified in cresyl violet–stained cross-sections. Sections were imaged by light microscopy, and RNFL thickness was quantified using ImageJ (National Institutes of Health, Bethesda, MD, USA). To standardize the measurement of the RNFL thickness, a line was drawn from the bottom of the outer nuclear layer to the top of the inner nuclear layer. This line was extended through the RNFL, where only the RNFL thickness was measured using ImageJ. This methodology allowed for the consistent and unbiased determination of where to measure the RNFL (Fig. 1). Experimental replicates represent an average of RNFL measurements across 16 longitudinal sections for each eye ($n = 3$ to 5 eyes per strain per time point).

Immunohistochemistry

IHC procedures were utilized as described previously.[54] Longitudinal sections through the ONH were sectioned and stained. The OCT compound was removed through two

washes in 1× PBS for 2 minutes each before the tissue was dried via subsequent washing in 70% ethanol for 2 minutes, then 100% ethanol for 2 minutes, and left to dry at room temperature for 10 minutes. Slides were washed in 1× PBS for 5 minutes, then incubated in 0.1% Triton X-100 at room temperature for 15 minutes to permeabilize the cell membranes. Slides were subsequently blocked for 1 hour at room temperature in SuperBlock Blocking Buffer (#37580; Thermo Fisher Scientific, Waltham, MA, USA) in PBS before being incubated at 4°C overnight in primary antibody: Anti-Fibronectin Antibody [IST-9], which binds the EDA domain (#ab6328, 1:100; Abcam, Cambridge, UK); Invitrogen Biglycan Polyclonal Antibody (#PA5-76821, 1:100; Thermo Fisher Scientific); Invitrogen RARA Polyclonal Antibody (#PA5-119640, 1:100; Thermo Fisher Scientific); Invitrogen IFN Gamma Polyclonal Antibody (#PA1-24782, 1:100; Thermo Fisher Scientific); and/or Invitrogen Phospho-STAT1 (Tyr701) Polyclonal Antibody (#44-376G, 1:100; Thermo Fisher Scientific).

Slides were then washed in 1× PBS for 5 minutes three times at room temperature before being incubated at room temperature for 1 hour in 2° antibody: Cy 3 AffiniPure Donkey Anti-Rabbit IgG (H+L) (1:200) and/or Cy 5 AffiniPure Donkey Anti-Mouse IgG (H+L) (#715175150, 1:200; Jackson ImmunoResearch). Slides were again washed in 1× PBS for 5 minutes three times at room temperature and mounted with Invitrogen ProLong Gold Antifade Mountant (Thermo Fisher Scientific) containing Invitrogen DAPI. Image acquisition was preformed using the ZEISS Axio Imager.Z2 microscope at 20×. ECM expression was measured as mean pixel intensity/area, represented as arbitrary units (AU) to account for ONH area variations between sections. ONH region was defined as starting from the inner nuclear layer just below the RNFL to just above the myelination zone, as determined by the morphological changes in the cells shown by the DAPI counterstain. The average mean pixel intensity across four to nine sections per eye was then calculated ($n = 4$ to 9 eyes per strain per time point). Scale bars represent 50 μm.

Laser Capture Microdissection

For LCM, 1.0-mm polyethylene naphthalate (PEN) membrane slides were prepared. To ensure that the PEN membrane slides were RNase free and to additionally sterilize the membrane slides, the membrane slides were incubated at 180°C for 4 hours as recommended by Zeiss. Then, 10-μm-thick frozen sections were mounted on previously treated PEN membrane slides with eight sections per slide, and two slides per eye were utilized for a total of 16 sections to account for the entire ONH. The slides were then stored at −80°C.

To visualize and map the ONH within each section, the sections were stained with cresyl violet as previously described and reiterated here.[64] Slides were stained and processed one slide at a time to prevent RNA degradation that begins to occur when sections are removed from −80°C storage. Each slide was placed in cold 75% EtOH for 30 seconds immediately after removal from the −80°C storage. Slides were then dipped in nuclease-free water for 10 to 15 seconds before ~300 μL of 1.5% cresyl violet in 75% EtOH was pipetted on them for 45 seconds at room temperature. Cresyl violet is known to not cause RNA degradation.[65] The tissue was then dehydrated in subsequent washes of 75%, 95%, and 100% EtOH in nuclease-free water for 30 seconds

each. Slides were air dried in a fume hood for 5 minutes before immediately moving on to laser capture.

LCM was performed with the ZEISS PALM CombiSystem. LCM cutting speed, microbeam laser energy level, and focus distance were optimized using control tissue from the mouse ONH sectioned at 10 μm to optimize settings prior to beginning the experiment. Laser cutting and catapulting were performed using PALMRobo V4.9 software. For laser cutting, we optimized the settings on a blank area near the sections. We followed the recommended laser cut and capture calibration process of the Cut Laser Adjustment Wizard in the Calibration section using a 20× objective. Initially, a low cutting speed was set at 5%, and we then fine-tuned the Energy and Focus parameters to achieve a clean cut. For laser catapulting of the cut section to the collection tube, we adjusted the Delta values for Energy and Focus under the LPC section. These adjustments ensured that the catapulting process effectively transferred cut pieces to the collection caps using the RoboLPC mode. Optimized settings were saved and used for all samples. The final optimized settings were as follows; cutting speed, 5%; Energy, 46%; Focus, 64; Delta Energy, 20; Delta Focus, 3. Automatic imaging to capture images of the ONH area before cut, after cut, and after ultraviolet laser dissection was implemented using the ZEISS PALM CombiSystem.

ONH segments from all sections from a single eye were collected in a 200-μL ZEISS Opaque AdhesiveCap within 1 hour after staining. Within each section, the ONH region was defined as starting from the inner nuclear layer just below the retinal nerve fiber layer to just above the myelination zone, determined by the morphological changes in the cells stained by cresyl violet, as well as reductions in stain intensity. Immediately after collection, 10 μL lysis buffer (RNeasy Plus Micro Kit, #74034; QIAGEN, Venlo, The Netherlands) was added into the upside-down adhesive cap containing each ONH section. After incubation at room temperature for 10 minutes, the cap was gently but tightly closed, and ONHs with lysis buffer were spun down. Collected samples were immediately processed through RNA extraction with the QIAGEN RNeasy Plus Micro Kit.

RNA-Seq, Read Alignment, and GSEA Analysis

RNA libraries were generated from total RNA isolated from the ONH ($n = 3$ to 5 ONHs per strain per time point). Total RNA was verified for purity and integrity using the NanoDrop One Spectrophotometer (Thermo Fisher Scientific) and Agilent 2100 Bioanalyzer (Agilent, Santa Clara, CA). RNA quality was assessed by both RNA integrity number (RIN) scores and 28S/18S ratios. As RIN scores are not always the best indicator of RNA quality and there is often great variability within and between samples,[66] we also considered the 28S/18S ratios to increase confidence in including samples. Although a 2:1 28S/18S ratio is often considered ideal, it has been reported that scores as low as 0.4 are adequate for hybridization and amplification.[67–69] Given these metrics, all of our samples met the minimum requirements for RNA quality (Supplemental Table S1).

Ultra-low RNA input libraries were generated using the Takara SMART-Seq v4 Ultra Low Input RNA Kit for Sequencing (Takara, Mountain View, CA, USA) for cDNA synthesis and the Nextera XT DNA library preparation (Illumina, San Diego, CA, USA) for cDNA dual indexing. Full-length

cDNA fragments are generated from 1 to 10 ng total RNA by the Takara SMART technology. cDNA fragments are fragmented and dual indexed in a single step by taking advantage of the simultaneous transposon and tagmentation step of the Nextera kit. Libraries were standardized to 2 nM. Paired-end 2 × 150 bp with 30M reads/sample sequencing was performed using standard sequencing by synthesis chemistry on an Illumina NovaSeq 6000 Sequencing System. Generated raw reads were quality controlled, aligned, and mapped to *Mus musculus* using Spliced Transcripts Alignment to a Reference (STAR),[70] followed by estimation of mapped pair-end reads using RNA-Seq by Expectation Maximization (RSEM).[71]

Gene Set Enrichment Analysis (GSEA) was performed by ranked enrichment analysis with MolSigDB (https://www.gsea-msigdb.org/gsea/msigdb, version 7.5.1). The subsequent ONH RNA-seq dataset was analyzed using recommendations from the GSEA tutorial for RNA-seq data (https://www.gsea-msigdb.org/gsea/doc/GSEAUserGuideFrame.html).[72] In this analysis, the adjusted P value (P_{adj}) was determined through Benjamini–Hochberg adjustments to account for multiple testing. Here, we used $P_{adj} < 0.20$ as our cutoff to generate GSEA groupings indicative of geneset enrichment.[72] Benjamini–Hochberg adjustments of P values allow for greater control of the false discovery rate (incidence of type I statistical errors), allowing for a more relaxed P_{adj} threshold by focusing on the proportion of false positives among the rejected hypothesis.[73] Using a P_{adj} of up to <0.25 as a cutoff in large datasets undergoing multiple testing is very common in gene expression analysis and RNA-seq profiling due to the massive amounts of data generated and compared.[73–75] Relaxing the P_{adj} threshold by utilizing a statistical analysis that helps control the false discovery rate enables the discovery of gene groupings that may have been missed due to the multiple testing. Because the GSEA analysis was utilized here as a hypothesis-generation procedure, we further examined the up- and downregulation of integral groupings that were shown to be changed between the B6.EDA^{+/+} mice and age-matched controls using IHC.

It is important to note that GSEA analysis does not determine the over- or under-expression of individual genes. Instead, it determines if biologically associated gene expression changes enable a specific grouping to be significantly up- or downregulated. Normalized enrichment scores (NESs) were used to quantify the magnitude of enrichment. Positive NES values indicate over-expression and negative NES values indicate under-expression of the entire group. Although there is no specific cut-off for a significant NES score, higher absolute NES values are considered indicative of a more significant biological response.[72]

Statistical Analysis

Statistical significance for IOP measurements, RGC counts, and IHC quantification were determined by unpaired Student's *t*-test. PPD stain statistical significance was determined by a Fisher's exact test and the Hommel post hoc method. All data represent mean value ± SEM. GSEA statistical analysis was performed by the University of Wisconsin–Madison Biotechnology Center for Bioinformatics Core Facility (Research Resource Identifier RRID:SCR_017799) as described above.

RESULTS

Here, we evaluated glaucomatous changes in the B6.EDA^{+/+} mouse model of ocular hypertension over the course of 22 months of age to define progressive damage in the retina and ONH. The B6.EDA^{+/+} mice had significantly elevated IOP compared to C57BL/6J controls that persisted through 22 months of age (Fig. 1A): at 12 months ($n = 12$ to 14 eyes/strain), C57BL/6J 13.2 ± 0.5 mmHg versus B6.EDA^{+/+} 17.1 ± 0.6 mmHg; at 22 months ($n = 16$ to 18 eyes/strain), C57BL/6J 11.9 ± 0.3 mmHg versus B6.EDA^{+/+} 14.6 ± 0.4 mmHg. In addition, B6.EDA^{+/+} mice had significant RGC loss compared to C57BL/6J controls at both 12 and 22 months (Fig. 1B, representative images Figs. 1C–F): at 12 months ($n = 3$ to 7 eyes/strain), C57BL/6J 3017 ± 136.7 RGCs/mm² versus B6.EDA^{+/+} 2458 ± 143.0 RGCs/mm²; at 22 months ($n = 3$ to 7 eyes/strain), C57BL/6J 2593 ± 124.0 RGCs/mm² versus B6.EDA^{+/+} 2055 ± 91.1 RGCs/mm². To further evaluate glaucomatous damage to the retina, we evaluated RNFL thickness using cresyl violet staining of the ONH region. The B6.EDA^{+/+} mice at both 12 months and 22 months of age had a significant decrease in RNFL thickness compared to age-matched C57BL/6J controls (Fig. 1H): at 12 months ($n = 3$ to 5 eyes/strain), C57BL/6J 62.0 ± 2.0 µm versus B6.EDA^{+/+} 39.8 ± 3.3 µm; at 22 months ($n = 3$ to 5 eyes/strain), C57BL/6J 68.5 ± 3.9 µm versus B6.EDA^{+/+} 44.1 ± 4.2 µm.

The B6.EDA^{+/+} mice had significantly increased ON damage compared to age-matched C57BL/6J controls at both 12 months ($P < 0.001$, $n = 13$ to 15 ONs/strain) and 22 months ($P < 0.01$, $n = 11$ to 13 ONs/strain) (Fig. 2A). Importantly, from 12 to 22 months of age, the ON damage significantly worsened in B6.EDA^{+/+} mice, indicating disease progression ($P < 0.01$) (Fig. 2A, representative images Figs. 2B–E).

Increases of ECM proteins in the ONH have been heavily implicated with glaucomatous pathophysiology.[42,44,76–79] Specifically, increases of the ECM proteins elastin; tenascin-c; collagens I, IV, V, and XI; proteoglycan; and FN have all been reported in the human glaucomatous ONH.[5,6,41,42,80–82] To elucidate ECM changes in the ONH of B6.EDA^{+/+} mice, immunohistochemical staining of the ONH at 12 months and 18 months of age was employed. The ECM protein and DAMP FN+EDA was significantly increased in the ONH of B6.EDA^{+/+} mice at both 12 months and 18 months of age compared to age-matched C57BL/6J controls (Fig. 3A): at 12 months ($n = 4$ to 9 eyes/strain), C57BL/6J 2157 ± 194.5 AU versus B6.EDA^{+/+} 3067 ± 331.1 AU; at 18 months ($n = 4$ to 9 eyes/strain), C57BL/6J 2886 ± 371.3 AU versus B6.EDA^{+/+} 5433 ± 551.2 AU. In addition, the ECM DAMP biglycan was significantly increased at 18 months of age (Fig. 3F): at 12 months ($n = 4$ to 6 eyes/strain), C57BL/6J 3995 ± 418.0 AU versus B6.EDA^{+/+} 4380 ± 285.7 AU; at 18 months ($n = 4$ to 6 eyes/strain), C57BL/6J 2904 ± 180.4 AU versus B6.EDA^{+/+} 5123 ± 634.4 AU in B6.EDA^{+/+} mice compared to age-matched C57BL/6J mice, whereas it was unchanged at 12 months of age. These data show progressive modifications to the ECM in the ONH region in B6.EDA^{+/+} mice over time.

To further elucidate changes in the transcriptome in the glaucomatous ONH of B6.EDA^{+/+} mice, we utilized LCM, a protocol that allows for highly pure tissue isolation,[64] to specifically isolate the ONH from the surrounding tissue (Figs. 4A, 4B). The entire ONH from a single sagittal cryosection was collected using LCM. The entire ONH
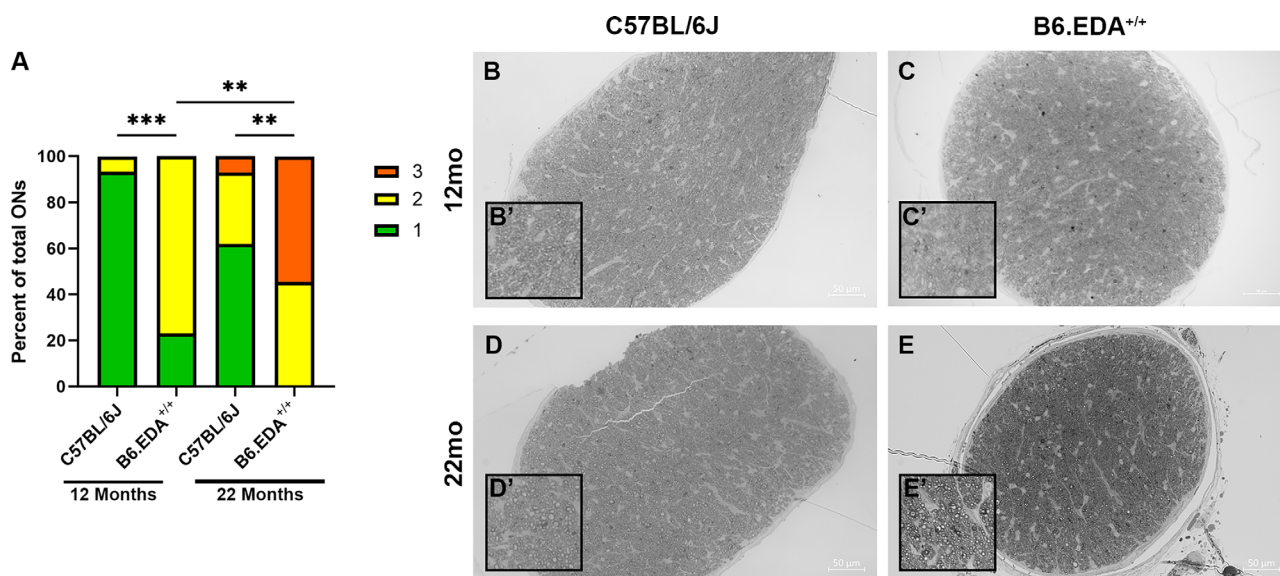
FIGURE 2. B6.EDA$^{+/+}$ mice showed progressive degradation of the ON from 12 months of age to 22 months of age. (**A**) B6.EDA$^{+/+}$ mice exhibited a higher percent of ON damage measured by PPD staining at 22 months of age compared to 12 months of age ($n = 11$ to 15 ONs per strain per time point). At 12 and 22 months of age, B6.EDA$^{+/+}$ mice demonstrated significantly increased ON damage compared to age-matched C57BL/6J controls. (**B–E**) Representative images of ON PPD staining at both 12 months and 22 months of age. Statistical significance was determined by Fisher's exact test and subsequent Hommel post hoc analysis for multiple comparisons. Data are presented as the percentage of total ONs measured ($n = 11$ to 15 ONs per strain per time point). **$P < 0.01$, ***$P < 0.001$.

across 16 sections was collected and pooled for each eye to represent one biological replicate ($n = 3$ to 5 eyes per strain per time point). This allowed for the collection of the entire three-dimensional ONH from each eye and isolation of RNA from a single ONH without having to pool biological replicates. Within each section, the ONH region was defined as starting from the inner nuclear layer just below the RNFL to the myelination zone, determined by the morphological changes in the cresyl violet staining. RNA was isolated from ONH sections for GSEA analysis of the ONH transcriptome between 12-month B6.EDA$^{+/+}$ mice and age-matched C57BL/6J controls, and between 22-month B6.EDA$^{+/+}$ mice and age-matched C57BL/6J controls (GEO Accession Number: GSE270934). NESs and adjusted P values were used as a standardized metric for determining significance to compare results across genesets.[72] Five GSEA-defined groups were significantly upregulated between B6.EDA$^{+/+}$ mice and C57BL/6J controls at 12 months of age (Fig. 4C, Supplemental Fig. S1). Four GSEA-defined groups were upregulated and four downregulated between B6.EDA$^{+/+}$ mice and age-matched C57BL/6J controls at 22 months of age (Fig. 4D, Supplemental Fig. S2). Across both time points, over 600 leading edge genes contributed to the significant changes in GSEA groupings (Figs. 4C, 4D). Leading-edge genes represent the main genes that account for the over- or under-representation of a predefined GSEA group. Tables show the NESs and adjusted P values of significantly changed GSEA groupings between B6.EDA$^{+/+}$ at 12 months (Fig. 4E) and 22 months (Fig. 4F) compared to age-matched C57BL/6J controls.

Consistent with the hypothesized role of the immune system in glaucoma disease progression, we observed significant increases in interferon (IFN) transcription at both 12 months and 22 months in B6.EDA$^{+/+}$ mice compared to age-matched C57BL/6J controls. These data support prior work that has implicated both IFNα and IFNγ signaling in glaucomatous pathophysiology in human patients[83-86] and

mouse models.[87] To quantify changes in IFNα and IFNγ at the protein level in B6.EDA$^{+/+}$ mice, we utilized immunohistochemical staining of the ONH region in 12-month-old and 18-month-old B6.EDA$^{+/+}$ mice and C57BL/6J age-matched controls. At 12 and 18 months of age, there were significant increases in IFNα in the ONH of B6.EDA$^{+/+}$ mice compared to C57BL/6J controls (Fig. 5A, representative images Figs. 5B–E): at 12 months ($n = 5$ to 9 eyes/strain), C57BL/6J 2870 ± 306.3 AU versus B6.EDA$^{+/+}$ 5289 ± 522.8 AU; at 18 months ($n = 5$ to 9 eyes/strain), C57BL/6J 2973 ± 246.0 AU versus B6.EDA$^{+/+}$ 4062 ± 367.8 AU. By 18 months of age, IFNγ was significantly increased in the ONH of B6.EDA$^{+/+}$ mice compared to C57BL/6J controls (Fig. 5F, representative images Figs. 5G–J): at 12 months ($n = 7$ to 9 eyes/strain), C57BL/6J 1147 ± 197.6 AU versus B6.EDA$^{+/+}$ 2074 ± 582.0 AU; at 18 months ($n = 7$ to 9 eyes/strain), C57BL/6J 809.9 ± 36.6 AU versus B6.EDA$^{+/+}$ 2120 ± 334.6 AU. These data suggest progressive changes to the glaucomatous ONH, as IFNα is known to be an early indicator of immune system activation, whereas IFNγ has been shown to be activated in later stages of disease, with evidence pointing toward increases through IFNα signaling.[88,89]

Further analysis of the 607 leading-edge genes generated from the GSEA analysis (Supplementary Excel Spreadsheet S1) identified signal transducer and activator of transcription (STAT) and downstream STAT signaling proteins, as part of the leading edge for each IFN GSEA group. Janus kinase (JAK), and subsequent STAT gene expression has been implicated in glaucoma disease progression in animal models.[90-93] Specifically, *STAT1* has been identified as a hub gene in two glaucoma mouse models: mice with *TDRD7* loss of function, and DBA/2J mice.[87,94,95] To quantify changes in phospho-STAT1 (pSTAT1) protein expression levels, the activated form of STAT1, we utilized immunohistochemical staining of the ONH region in 12-month-old and 18-month-old B6.EDA$^{+/+}$ mice and C57BL/6J age-matched controls. At 18 months of age, there were significant increases in pSTAT1
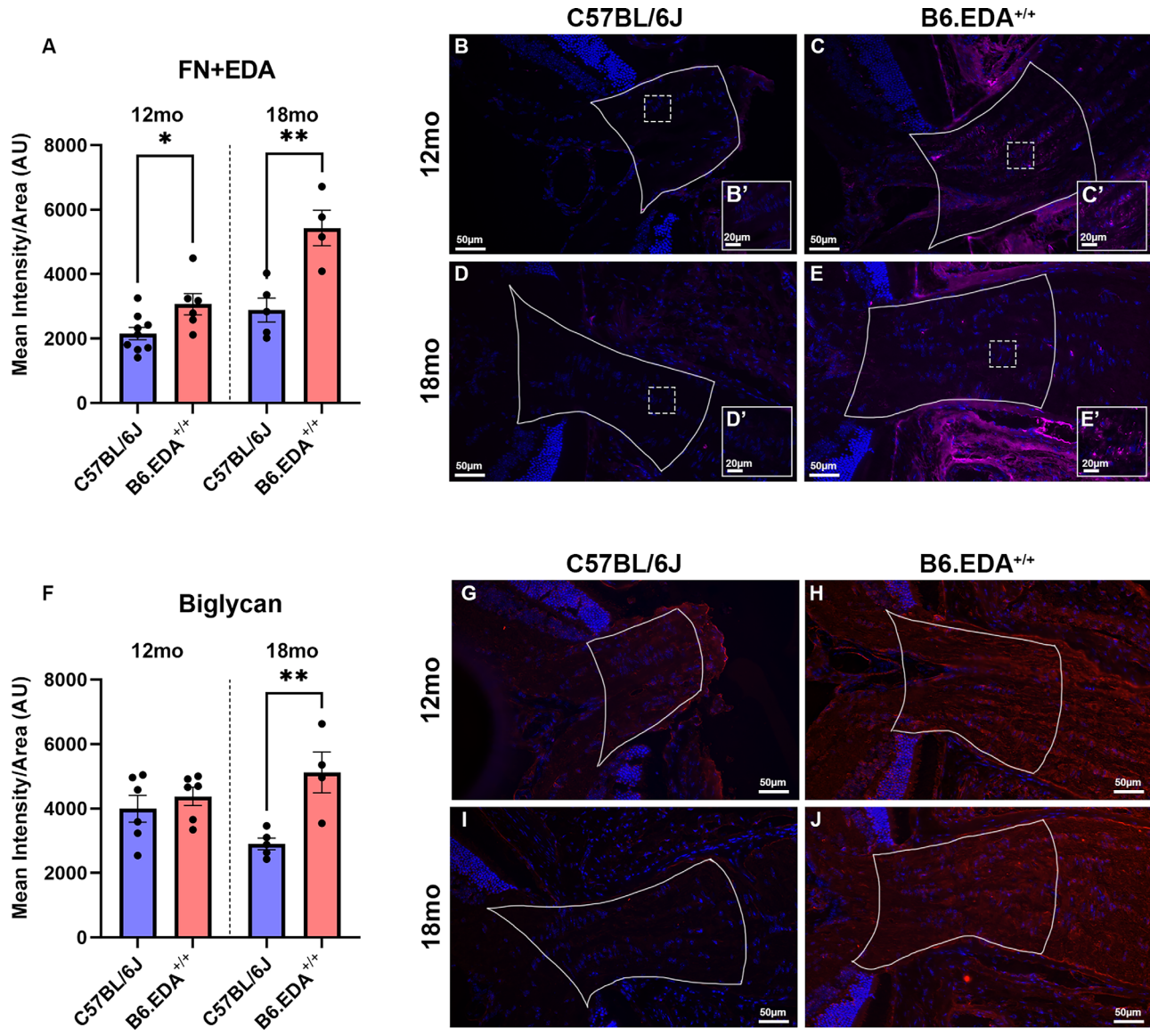
Figure 3. B6.EDA$^{+/+}$ mice showed increased DAMP expression in the ONH. (**A**) FN+EDA expression was significantly increased in the ONH at 12 months and 18 months of age in B6.EDA$^{+/+}$ mice compared to age-matched controls ($n = 4$ to 9 eyes/strain). (**B–E**) Representative images of FN+EDA expression in B6.EDA$^{+/+}$ at 12 months and 18 months of age (**C**, **E**) compared to age-matched controls (**B**, **D**). (**F**) Biglycan expression was significantly increased in the ONH at 18 months in B6.EDA$^{+/+}$ mice compared to age-matched controls ($n = 4$ to 6 eyes/strain). (**G–J**) Representative images of biglycan expression in B6.EDA$^{+/+}$ at 12 months and 18 months of age (**H**, **J**) compared to age-matched controls (**G**, **I**). *White lines* outline the measured ONH section of images. *Dashed boxes* represent location of $40\times$ imaging of FN+EDA, as shown in the inserts (**B'–E'**). *Scale bar*: 50 μm, unless otherwise stated. Significance was determined by Student's *t*-test. $P < 0.05$, **$P < 0.01$.

protein expression in the ONH of B6.EDA$^{+/+}$ mice compared to C57BL/6J controls (Fig. 6A, representative images Figs. 6B–6E): at 12 months ($n = 6$ to 9 eyes/strain), C57BL/6J 2228 ± 137.5 AU versus B6.EDA$^{+/+}$ 2328 ± 125.2 AU; at 18 months ($n = 6$ to 9 eyes/strain), C57BL/6J 2040 ± 128.3 AU versus B6.EDA$^{+/+}$ 2675 ± 225.1 AU. These data support time-dependent and progressive changes to IFN and subsequent STAT signaling in glaucomatous disease progression.

Discussion

In primary open-angle glaucoma, activation of the immune system has been heavily implicated in disease progression and pathophysiology.[9,18–20] However, the pathogenic signaling pathways responsible for these immune and fibrotic changes are not fully understood. Mice are genetically similar to humans with comparable anatomy, making them an ideal model system to study glaucoma phenotypes and ONH pathophysiology.[96,97] Previously, we have utilized several transgenic mouse lines to show that constitutively active FN+EDA mice (B6.EDA$^{+/+}$) develop ocular hypertension and exhibit glaucomatous damage by 1 year of age, and these phenotypes are dependent on TLR4 signaling.[7,54] Here, we further investigated the roles of DAMPs, activators of TLR4, and downstream fibro-inflammatory signaling in the development and progression of glaucomatous damage. In addition, we explored the transcriptomic changes at 12 and
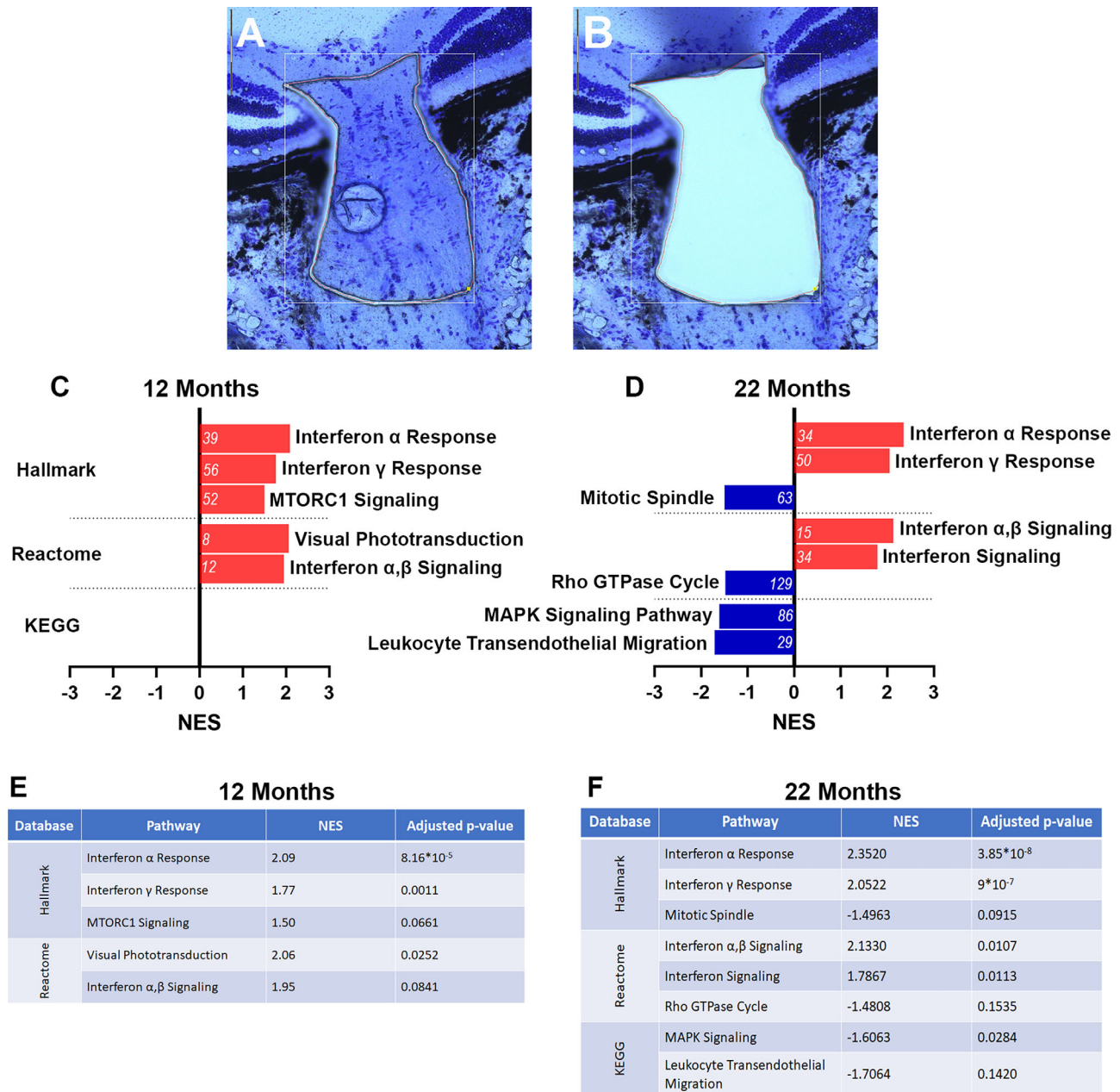
FIGURE 4. Up- and downregulated genesets in the ONH of B6.EDA$^{+/+}$ mice. The ONH of 12-month-old ($n = 4$ to 5 eyes) and 22-month-old ($n = 3$ to 5 eyes) mice were isolated using LCM before undergoing RNA isolation, cDNA library preparation, and subsequent GSEA analysis. The ONH region was defined as starting from the inner nuclear layer just below the RNFL down to the myelination zone, determined by the morphological changes in the hematoxylin and eosin (H&E) staining. (**A**, **B**) The ONH was outlined by hand (**A**) and isolated (**B**) for subsequent processing. GSEA analysis showed significant increases in various signaling pathways across three different pathway databases: hallmark, reactome, and KEGG. Numbers within bars represent the number of leading-edge genes. (**C**) At 12 months of age, B6.EDA$^{+/+}$ mice had significantly increased expression of genes related to IFNα, IFNγ, MTORC1, visual phototransduction, and IFNα,β signaling from the hallmark and reactome databases. No differences were found between B6.EDA$^{+/+}$ and C57BL/6J RNA expression in the KEGG database at 12 months of age. (**D**) At 22 months of age, B6.EDA$^{+/+}$ mice had statistically significant increased expression of genes related to IFNα response, IFNγ response, IFNα,β signaling, and IFN signaling (*red bars*). There were also statistically significant decreases in the expression of genes related to mitotic spindle signaling, the rho GTPase cycle, MAPK signaling pathway, and leukocyte transendothelial migration (*blue bars*). *White numbers* represent total number of leading-edge genes (see Supplementary Excel Spreadsheet S1). (**E**) Tables showing the NESs and adjusted P values for upregulated GSEA groups between B6.EDA$^{+/+}$ at 12 months and age-matched C57BL/6J controls. (**F**) Tables showing the NESs and adjusted P values for upregulated GSEA groups between B6.EDA$^{+/+}$ at 22 months and age-matched C57BL/6J controls.
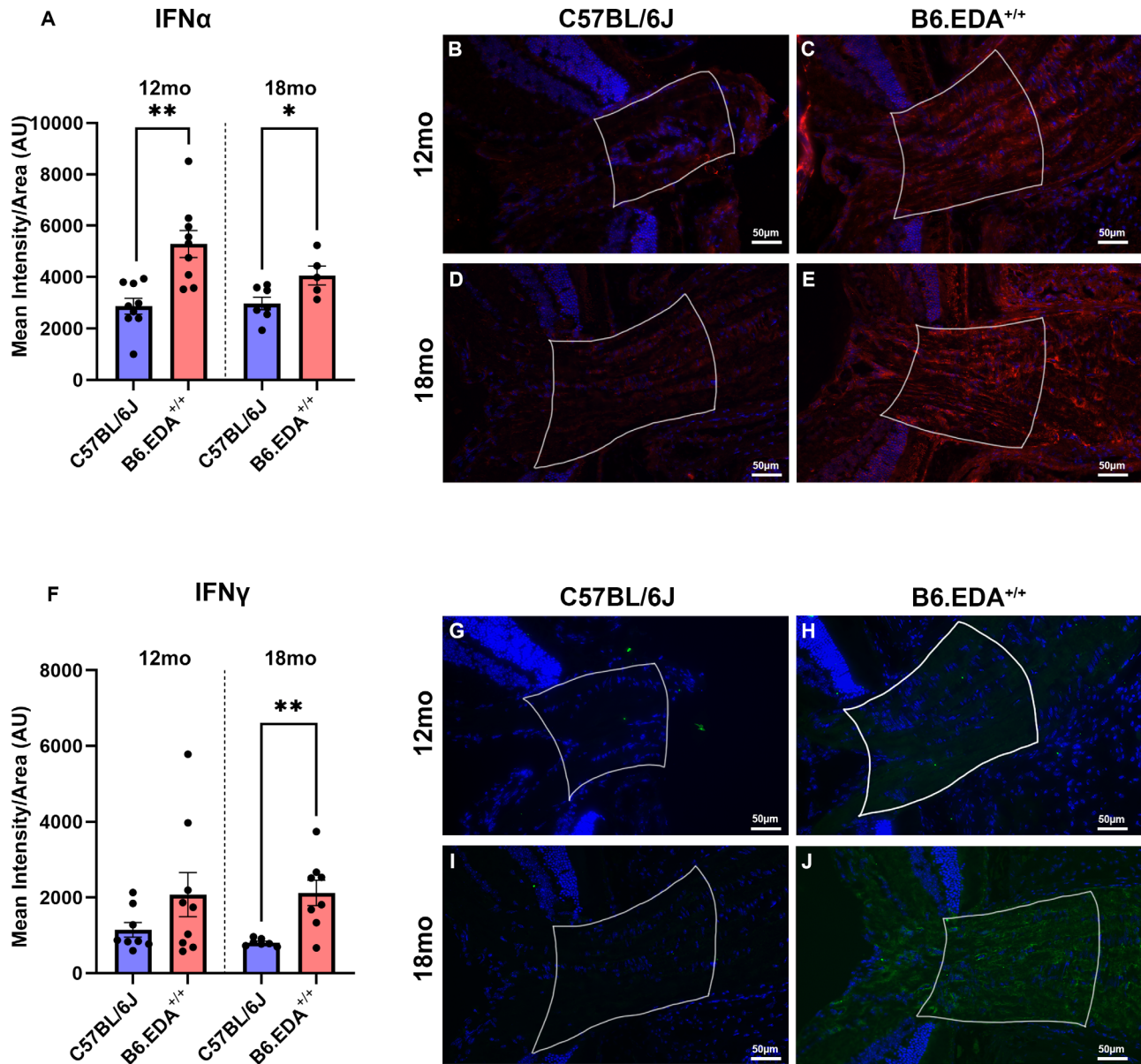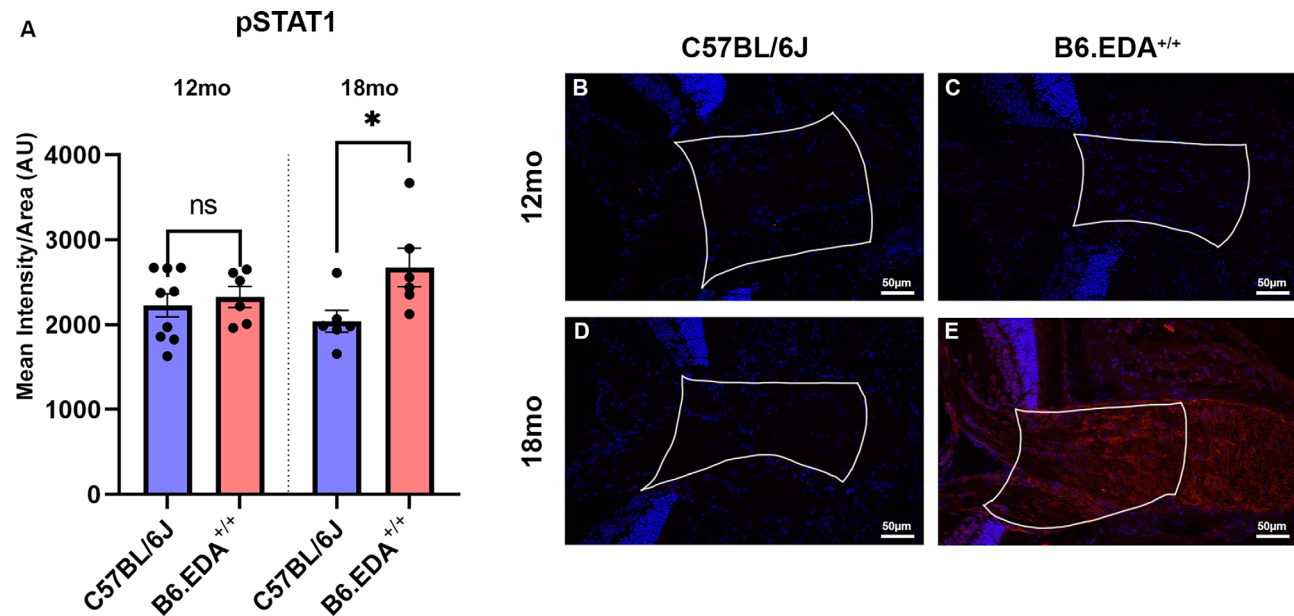
FIGURE 5. B6.EDA$^{+/+}$ mice showed increased IFNα and IFNγ protein expression in the ONH. (**A**) IFNα expression was significantly increased in the ONH at 12 months and 18 months of age in B6.EDA$^{+/+}$ mice compared to age-matched controls ($n = 5$ to 9 eyes/strain). (**B–E**) Representative images of IFNα expression in B6.EDA$^{+/+}$ at 12 months and 18 months of age (**C**, **E**) compared to age-matched controls (**B**, **D**). (**F**) IFNγ expression was significantly increased in the ONH at 18 months but not 12 months of age in B6.EDA$^{+/+}$ mice compared to age-matched controls ($n = 7$ to 9 eyes/strain). (**G–J**) Representative images of IFNγ expression in B6.EDA$^{+/+}$ at 12 months and 18 months of age (**H**, **J**) compared to age-matched controls (**G**, **I**). *White lines* outline the measured ONH section of images. Significance was determined by Student's *t*-test. *$P < 0.05$, **$P < 0.01$.

22 months of age to further elucidate signaling mechanisms responsible for the development of progressive glaucomatous damage.

To further investigate glaucomatous damage in B6.EDA$^{+/+}$ mice, we used a battery of testing parameters that have previously been used to define damage progression, including IOP measurements, RGC loss, RNFL thickness, and ON damage scores.[7,44,54,57,58,60,61,98,99] We demonstrated that IOP remains significantly increased through 22 months of age in B6.EDA$^{+/+}$ mice (Fig. 1A), leading to significant RGC loss (Fig. 1B) and decreases in RNFL thickness (Fig. 1H). Interestingly, the loss of RGCs and RNFL thickness does not significantly progress through this

time course. However, ON damage did significantly worsen from 12 months to 22 months in the B6.EDA$^{+/+}$ mice (Fig. 2A). This progression of disease severity indicates a continual effect of ocular hypertension on ON damage and further suggests that the initial site of damage is occurring in the ON, as is known to occur in the pathophysiology of glaucoma.

Previously, we and others identified that DAMP expression is increased in the human glaucomatous ONH compared to healthy individuals.[6,40–42] In addition, DAMP activation of TLR4 has been shown to significantly increase fibrosis in human primary trabecular meshwork cells[44] and hONH LC cells.[42] Previously, we have shown that TLR4

FIGURE 6. B6.EDA$^{+/+}$ mice showed increased protein expression of pSTAT1 in the ONH at 18 months of age. (**A**) pSTAT1 expression was significantly increased in the ONH at 18 months of age in B6.EDA$^{+/+}$ mice but not at 12 months compared to age-matched controls ($n = 6$ to 9 eyes/strain). (**B–E**) Representative images of pSTAT1 expression in B6.EDA$^{+/+}$ at 12 months and 18 months of age (**C, E**) compared to age-matched controls (**B, D**). *White lines* outline the measured ONH section of images. Significance was determined by Student's *t*-test. *$P < 0.05$.

signaling is necessary for DAMP-induced IOP elevation and trabecular meshwork damage, as well as fibrotic changes to LC cells in culture, suggesting that the innate immune system is a mechanism for glaucoma damage.[42,54] TLR4 signaling has also been implicated in initiating fibrotic responses in several other fibrotic disease states such as scleroderma,[100] liver disease,[101] and kidney disease,[102] highlighting the importance and relevance of this signaling pathway.[100,103,104] Here, we have shown that the DAMP FN+EDA is significantly elevated at both 12 months and 18 months of age (Fig. 3A), and we also observed significantly higher levels of the DAMP biglycan by 18 months of age in B6.EDA$^{+/+}$ mice (Fig. 3F). FN+EDA is known to amplify TGFβ2-dependent ECM responses in human TM cells, as well as human ONH LC cells,[42,44] suggesting a mechanism by which DAMPs are modulating the ONH region in glaucoma. It is known FN+EDA is expressed by glial cells[105]. We observed significant increases of FN+EDA protein expression in the mouse ONH (Fig. 3A), which lacks the LC cell population, suggesting that astrocytes and/or microglia are the likely source of FN+EDA. Along with FN+EDA, biglycan is a known proinflammatory signaling molecule that acts as a DAMP, activating TLR4 signaling.[35,106] Biglycan primarily supports tissues when exposed to compressional forces,[107] and it has been shown to be upregulated in human ONH LC cell cultures after mechanical stress.[36] Interesting, biglycan expression was significantly increased at 18 months of age in the B6.EDA$^{+/+}$ ONH, but not at 12 months, suggesting a time-dependent increase in this DAMP, likely related to prolonged mechanical stress and strain on the ONH. It is important to note that mice do not have LC cells; instead, the lamina region is formed and occupied by resident astrocytes and microglia. Thus, these data suggest a time-sensitive role of astrocyte- and microglia-produced DAMPs in progressive glaucomatous pathophysiology. Although biglycan is known to be expressed in human ONH LC cells, it remains to be

determined if expression levels are significantly different in the human glaucomatous ONH.[108] These data suggest a continued response to the elevated IOP, implicated by time-specific responses to the production of various ECM and DAMP molecules. These data identify B6.EDA$^{+/+}$ mice as a novel model of open-angle glaucoma with slowly progressive damage to the retina, ONH, and ON. One caveat of the B6.EDA$^{+/+}$ model is that FN+EDA is constitutively expressed in all tissues, meaning that, when FN is produced, it always contains the EDA domain. Therefore, it is possible that the molecular changes occurring could be due to ocular hypertension alone and/or the constitutive expression of FN+EDA in the ONH. However, previous work in the IOP-dependent DBA/2J mouse model of glaucoma has indicated similar glaucomatous damage and molecular changes in the ONH.[61,109,110] In addition, we have previously reported that, in the B6.EDA$^{+/+}$ model, elevated IOP begins at 14 weeks of age with RGC loss and ON damage not occurring until 12 months of age.[7,54] These data suggest that the glaucomatous damage is likely due to prolonged ocular hypertension.

To further elucidate the complicated signaling pathways underlying the progressive glaucomatous phenotypes, we performed transcriptomic profiling to gain a comprehensive insight to the progressive changes occurring within the ONH. The ONH was harvested using LCM, a protocol that allows for highly pure tissue isolation.[64] We identified significant upregulation and downregulation of various signaling groupings using GSEA analysis across three different databases: hallmark, reactome, and Kyoto Encyclopedia of Genes and Genomes (KEGG; https://www.gsea-msigdb.org/gsea/doc/GSEAUserGuideFrame.html) (Figs. 4C, 4D). Significant increases of immune system IFNα, IFNβ, and IFNγ signaling indicated highly enriched gene groupings at both 12 months and 22 months of age (Figs. 4C, 4D). This is consistent with the known role of the immune system in glaucoma disease progression.[9,18]

Interferons are crucial inflammatory signaling molecules. IFNα and IFNγ levels are known to be significantly increased in the glaucomatous AH and serum levels in human patients.[83,85,111,112] Interestingly, the increased serum IFNγ levels negatively correlated with RNFL thickness, indicating a pathological role of IFN signaling in RGC loss.[83] In human ONH astrocyte cell cultures, stimulation with IFNγ was sufficient to upregulate astrogliosis and immune system markers.[113] Here, we were able to implicate the pathophysiological role of IFN signaling in the glaucomatous ONH specifically. RNA-seq identified the important signaling pathways that are differentially expressed. Utilizing IHC methodology allowed us to confirm significant findings on a protein level ($n = 4$ or 5 biological replicates per experimental group). Subsequent protein expression analysis indicated a time-specific response to the IFN family, specifically IFNα and IFNγ (Figs. 5A, 5F). These data suggest a direct role of IFN signaling in the glaucomatous ONH, where the majority of RGC axonal damage occurs.[2,3]

Further analysis of leading-edge genes in the IFN signaling GSEA groups showed that JAK/STAT genes, specifically *Stat1* and *Stat3*, and downstream JAK/STAT genes were included in the leading-edge gene sets for all IFN groups at both time points (Supplementary Excel Spreadsheet S1). IFNs initiate rapid pro-inflammatory signaling primarily through the JAK/STAT pathways. STAT1 has previously been identified as a hub gene in two mouse models of glaucoma,[87] with downstream STAT1 proteins upregulated in various mouse models of ON damage.[90,91,114] Downstream signaling of STAT1 has also been implicated in increased immune activation in hONH astrocyte cell cultures, as well as rodent models of glaucoma.[115–119] We demonstrated that pSTAT1 protein expression, the activated form of STAT1, was significantly upregulated at 18 months in our glaucoma model but not at 12 months (Fig. 6A). This suggests that activation of the JAK/STAT pathway in the glaucomatous ONH is a late-onset response to the glaucomatous ONH damage and chronic ocular hypertension, rather than an initiating mechanism of early damage. Future studies are needed to identify signaling mechanisms of the JAK/STAT pathway in relation of IFN signaling. Although we were able to identify these inflammatory pathways and potential downstream signaling proteins that change significantly, it is important to note that our RNA-seq analysis was based on only three to five biological replicates. Due to this low sample size, other signaling pathways that are changing and contributing to the glaucomatous damage may have been missed, such as axonal-related pathways, as well as the significant fibrotic and DAMP protein level changes that were discovered utilizing IHC methodologies. Also, this LCM methodology did not allow for the harvesting of individual cell populations (e.g., astrocytes only), enabling us to focus on global ONH changes. Future experiments will further explore other global changes, as well as single-cell or single-cell–type contributions to the glaucomatous ONH damage.

Conclusions

In summary, these data show the development of slowly progressive glaucomatous damage in a novel mouse model over 2 years. These data also point to a new method of measuring RNFL thickness using histology. To the best of our knowledge, we are the first to demonstrate integral changes of IFN signaling and the JAK/STAT pathway throughout disease progression in the ONH in response to ocular hypertension. Importantly, there are time-specific responses in DAMP production, IFN signaling activation, and pSTAT1 expression in the glaucomatous ONH, indicating possible novel therapeutic targets to treat and manage glaucoma disease progression. Thus, these data indicate that the progressive glaucomatous damage in the ON of B6.EDA$^{+/+}$ mice is driven by a pro-inflammatory signaling cascade.

References

1. Aboobakar IF, Wiggs JL. The genetics of glaucoma: disease associations, personalised risk assessment and therapeutic opportunities–a review. *Clin Exp Ophthalmol*. 2022;50:143–162.
2. Weinreb RN, Aung T, Medeiros FA. The pathophysiology and treatment of glaucoma. *JAMA*. 2014;311:1901–1911.
3. Weinreb RN, Leung CK, Crowston JG, et al. Primary open-angle glaucoma. *Nat Rev Dis Primers*. 2016;2:16067.
4. Hernandez MR. The optic nerve head in glaucoma: role of astrocytes in tissue remodeling. *Prog Retin Eye Res*. 2000;19:297–321.
5. Hernandez MR, Andrzejewska WM, Neufeld AH. Changes in the extracellular matrix of the human optic nerve head in primary open-angle glaucoma. *Am J Ophthalmol*. 1990;109:180–188.
6. Pena JD, Netland PA, Vidal I, Dorr DA, Rasky A, Hernandez MR. Elastosis of the lamina cribrosa in glaucomatous optic neuropathy. *Exp Eye Res*. 1998;67:517–524.
7. Mavlyutov TA, Myrah JJ, Chauhan AK, Liu Y, McDowell CM. Fibronectin extra domain A (FN-EDA) causes glaucomatous trabecular meshwork, retina, and optic nerve damage in mice. *Cell Biosci*. 2022;12:72.
8. Morrison JC, Cepurna Ying Guo WO, Johnson EC. Pathophysiology of human glaucomatous optic nerve damage: insights from rodent models of glaucoma. *Exp Eye Res*. 2011;93:156–164.
9. Baudouin C, Kolko M, Melik-Parsadaniantz S, Messmer EM. Inflammation in glaucoma: from the back to the front of the eye, and beyond. *Prog Retin Eye Res*. 2021;83:100916.

10. Tezel G. The immune response in glaucoma: a perspective on the roles of oxidative stress. *Exp Eye Res*. 2011;93:178–186.

11. Ramirez AI, de Hoz R, Salobrar-Garcia E, et al. The role of microglia in retinal neurodegeneration: alzheimer's disease, Parkinson, and glaucoma. *Front Aging Neurosci*. 2017;9:214.

12. Bosco A, Crish SD, Steele MR, et al. Early reduction of microglia activation by irradiation in a model of chronic glaucoma. *PLoS One*. 2012;7:e43602.

13. Quigley HA, Addicks EM, Green WR, Maumenee AE. Optic nerve damage in human glaucoma. II. The site of injury and susceptibility to damage. *Arch Ophthalmol*. 1981;99:635–649.

14. Morgan JE. Circulation and axonal transport in the optic nerve. *Eye (Lond)*. 2004;18:1089–1095.

15. Zode GS, Clark AF, Wordinger RJ. Activation of the BMP canonical signaling pathway in human optic nerve head tissue and isolated optic nerve head astrocytes and lamina cribrosa cells. *Invest Ophthalmol Vis Sci*. 2007;48:5058–5067.

16. Zode GS, Clark AF, Wordinger RJ. Bone morphogenetic protein 4 inhibits TGF-β2 stimulation of extracellular matrix proteins in optic nerve head cells: role of gremlin in ECM modulation. *Glia*. 2009;57:755–766.

17. Zode GS, Sethi A, Brun-Zinkernagel AM, Chang IF, Clark AF, Wordinger RJ. Transforming growth factor-β2 increases extracellular matrix proteins in optic nerve head cells via activation of the Smad signaling pathway. *Mol Vis*. 2011;17:1745–1758.

18. Vohra R, Tsai JC, Kolko M. The role of inflammation in the pathogenesis of glaucoma. *Surv Ophthalmol*. 2013;58:311–320.

19. Rieck J. The pathogenesis of glaucoma in the interplay with the immune system. *Invest Ophthalmol Vis Sci*. 2013;54:2393–2409.

20. Rolle T, Ponzetto A, Malinverni L. The role of neuroinflammation in glaucoma: an update on molecular mechanisms and new therapeutic options. *Front Neurol*. 2020;11:612422.

21. Sierra A, Encinas JM, Deudero JJ, et al. Microglia shape adult hippocampal neurogenesis through apoptosis-coupled phagocytosis. *Cell Stem Cell*. 2010;7:483–495.

22. Cuenca N, Fernandez-Sanchez L, Campello L, et al. Cellular responses following retinal injuries and therapeutic approaches for neurodegenerative diseases. *Prog Retin Eye Res*. 2014;43:17–75.

23. Hanisch UK, Kettenmann H. Microglia: active sensor and versatile effector cells in the normal and pathologic brain. *Nat Neurosci*. 2007;10:1387–1394.

24. Raivich G, Bohatschek M, Kloss CU, Werner A, Jones LL, Kreutzberg GW. Neuroglial activation repertoire in the injured brain: graded response, molecular mechanisms and cues to physiological function. *Brain Res Brain Res Rev*. 1999;30:77–105.

25. Nimmerjahn A, Kirchhoff F, Helmchen F. Resting microglial cells are highly dynamic surveillants of brain parenchyma in vivo. *Science*. 2005;308:1314–1318.

26. Davalos D, Grutzendler J, Yang G, et al. ATP mediates rapid microglial response to local brain injury in vivo. *Nat Neurosci*. 2005;8:752–758.

27. Prinz M, Jung S, Priller J. Microglia biology: one century of evolving concepts. *Cell*. 2019;179:292–311.

28. Liddelow SA, Guttenplan KA, Clarke LE, et al. Neurotoxic reactive astrocytes are induced by activated microglia. *Nature*. 2017;541:481–487.

29. Geiduschek EK, McDowell CM. The fibro-inflammatory response in the glaucomatous optic nerve head. *Int J Mol Sci*. 2023;24:13240.

30. Takano Y, Shi D, Shimizu A, et al. Association of Toll-like receptor 4 gene polymorphisms in Japanese subjects with primary open-angle, normal-tension, and exfoliation glaucoma. *Am J Ophthalmol*. 2012;154:825–832.e1.

31. Navarro-Partida J, Alvarado Castillo B, Martinez-Rizo AB, Rosales-Diaz R, Velazquez-Fernandez JB, Santos A. Association of single-nucleotide polymorphisms in non-coding regions of the *TLR4* gene with primary open angle glaucoma in a Mexican population. *Ophthalmic Genet*. 2017;38:325–329.

32. Shibuya E, Meguro A, Ota M, et al. Association of Toll-like receptor 4 gene polymorphisms with normal tension glaucoma. *Invest Ophthalmol Vis Sci*. 2008;49:4453–4457.

33. Kawai T, Akira S. The role of pattern-recognition receptors in innate immunity: update on Toll-like receptors. *Nat Immunol*. 2010;11:373–384.

34. Miyake K. Innate immune sensing of pathogens and danger signals by cell surface Toll-like receptors. *Semin Immunol*. 2007;19:3–10.

35. Piccinini AM, Midwood KS. DAMPening inflammation by modulating TLR signalling. *Mediators Inflamm*. 2010;2010:672395.

36. Kirwan RP, Fenerty CH, Crean J, Wordinger RJ, Clark AF, O'Brien CJ. Influence of cyclical mechanical strain on extracellular matrix gene expression in human lamina cribrosa cells in vitro. *Mol Vis*. 2005;11:798–810.

37. Kumar V. Toll-like receptors in the pathogenesis of neuroinflammation. *J Neuroimmunol*. 2019;332:16–30.

38. Tarassishin L, Suh HS, Lee SC. LPS and IL-1 differentially activate mouse and human astrocytes: role of CD14. *Glia*. 2014;62:999–1013.

39. Hernandez MR, Agapova OA, Yang P, Salvador-Silva M, Ricard CS, Aoi S. Differential gene expression in astrocytes from human normal and glaucomatous optic nerve head analyzed by cDNA microarray. *Glia*. 2002;38:45–64.

40. Luo C, Yang X, Kain AD, Powell DW, Kuehn MH, Tezel G. Glaucomatous tissue stress and the regulation of immune response through glial Toll-like receptor signaling. *Invest Ophthalmol Vis Sci*. 2010;51:5697–5707.

41. Pena JD, Varela HJ, Ricard CS, Hernandez MR. Enhanced tenascin expression associated with reactive astrocytes in human optic nerve heads with primary open angle glaucoma. *Exp Eye Res*. 1999;68:29–40.

42. Geiduschek EK, Milne PD, Mzyk P, Mavlyutov TA, McDowell CM. TLR4 signaling modulates extracellular matrix production in the lamina cribrosa. *Front Ophthalmol (Lausanne)*. 2022;2:968381.

43. Acott TS, Kelley MJ. Extracellular matrix in the trabecular meshwork. *Exp Eye Res*. 2008;86:543–561.

44. Hernandez H, Medina-Ortiz WE, Luan T, Clark AF, McDowell CM. Crosstalk between transforming growth factor beta-2 and Toll-like receptor 4 in the trabecular meshwork. *Invest Ophthalmol Vis Sci*. 2017;58:1811–1823.

45. Wordinger RJ, Fleenor DL, Hellberg PE, et al. Effects of TGF-β2, BMP-4, and gremlin in the trabecular meshwork: implications for glaucoma. *Invest Ophthalmol Vis Sci*. 2007;48:1191–1200.

46. Faralli JA, Filla MS, Peters DM. Role of fibronectin in primary open angle glaucoma. *Cells*. 2019;8:1518.

47. White ES, Baralle FE, Muro AF. New insights into form and function of fibronectin splice variants. *J Pathol*. 2008;216:1–14.

48. Ffrench-Constant C. Alternative splicing of fibronectin—many different proteins but few different functions. *Exp Cell Res*. 1995;221:261–271.

49. Muro AF, Chauhan AK, Gajovic S, et al. Regulated splicing of the fibronectin EDA exon is essential for proper skin wound healing and normal lifespan. *J Cell Biol*. 2003;162:149–160.

50. Kuhn C, 3rd, Boldt J, King TE, Jr, Crouch E, Vartio T, McDonald JA. An immunohistochemical study of architectural remodeling and connective tissue synthesis in pulmonary fibrosis. *Am Rev Respir Dis*. 1989;140:1693–1703.

51. Ffrench-Constant C, Van de Water L, Dvorak HF, Hynes RO. Reappearance of an embryonic pattern of fibronectin splicing during wound healing in the adult rat. *J Cell Biol*. 1989;109:903–914.

52. Hino K, Shiozawa S, Kuroki Y, et al. EDA-containing fibronectin is synthesized from rheumatoid synovial fibroblast-like cells. *Arthritis Rheum*. 1995;38:678–683.

53. Medina-Ortiz WE, Belmares R, Neubauer S, Wordinger RJ, Clark AF. Cellular fibronectin expression in human trabecular meshwork and induction by transforming growth factor-β2. *Invest Ophthalmol Vis Sci*. 2013;54:6779–6788.

54. Roberts AL, Mavlyutov TA, Perlmutter TE, et al. Fibronectin extra domain A (FN-EDA) elevates intraocular pressure through Toll-like receptor 4 signaling. *Sci Rep*. 2020;10:9815.

55. Howell GR, Libby RT, Marchant JK, et al. Absence of glaucoma in DBA/2J mice homozygous for wild-type versions of *Gpnmb* and *Tyrp1*. *BMC Genet*. 2007;8:45.

56. Mao M, Hedberg-Buenz A, Koehn D, John SW, Anderson MG. Anterior segment dysgenesis and early-onset glaucoma in *nee* mice with mutation of *Sh3pxd2b*. *Invest Ophthalmol Vis Sci*. 2011;52:2679–2688.

57. McDowell CM, Luan T, Zhang Z, et al. Mutant human myocilin induces strain specific differences in ocular hypertension and optic nerve damage in mice. *Exp Eye Res*. 2012;100:65–72.

58. Pang IH, Clark AF. Rodent models for glaucoma retinopathy and optic neuropathy. *J Glaucoma*. 2007;16:483–505.

59. Anderson DR, Normal Tension Glaucoma Study. Collaborative normal tension glaucoma study. *Curr Opin Ophthalmol*. 2003;14:86–90.

60. Chauhan BC, Levatte TL, Garnier KL, et al. Semiquantitative optic nerve grading scheme for determining axonal loss in experimental optic neuropathy. *Invest Ophthalmol Vis Sci*. 2006;47:634–640.

61. Libby RT, Anderson MG, Pang IH, et al. Inherited glaucoma in DBA/2J mice: pertinent disease features for studying the neurodegeneration. *Vis Neurosci*. 2005;22:637–648.

62. Maes ME, Donahue RJ, Schlamp CL, Marola OJ, Libby RT, Nickells RW. BAX activation in mouse retinal ganglion cells occurs in two temporally and mechanistically distinct steps. *Mol Neurodegener*. 2023;18:67.

63. Wurl JA, Mac Nair CE, Dietz JA, Shestopalov VI, Nickells RW. Contralateral astrocyte response to acute optic nerve damage is mitigated by PANX1 channel activity. *Int J Mol Sci*. 2023;24:15641.

64. Sutherland C, Wang Y, Brown RV, et al. Laser capture microdissection of highly pure trabecular meshwork from mouse eyes for gene expression analysis. *J Vis Exp*. 2018;136:57576.

65. Clement-Ziza M, Munnich A, Lyonnet S, Jaubert F, Besmond C. Stabilization of RNA during laser capture microdissection by performing experiments under argon atmosphere or using ethanol as a solvent in staining solutions. *RNA*. 2008;14:2698–2704.

66. Sonntag KC, Tejada G, Subburaju S, Berretta S, Benes FM, Woo TU. Limited predictability of postmortem human brain tissue quality by RNA integrity numbers. *J Neurochem*. 2016;138:53–59.

67. Ashton MN, Worsham AE, Strawn MD, et al. Degraded RNA from human anterior cruciate ligaments yields valid gene expression profiles. *Int J Mol Sci*. 2023;24:1895.

68. Diskin S, Kumar J, Cao Z, et al. Detection of differentially expressed glycogenes in trabecular meshwork of eyes with primary open-angle glaucoma. *Invest Ophthalmol Vis Sci*. 2006;47:1491–1499.

69. Skrypina NA, Timofeeva AV, Khaspekov GL, Savochkina LP, Beabealashvili R. Total RNA suitable for molecular biology analysis. *J Biotechnol*. 2003;105:1–9.

70. Dobin A, Davis CA, Schlesinger F, et al. STAR: ultrafast universal RNA-seq aligner. *Bioinformatics*. 2013;29:15–21.

71. Li B, Dewey CN. RSEM: accurate transcript quantification from RNA-seq data with or without a reference genome. *BMC Bioinformatics*. 2011;12:323.

72. Subramanian A, Tamayo P, Mootha VK, et al. Gene set enrichment analysis: a knowledge-based approach for interpreting genome-wide expression profiles. *Proc Natl Acad Sci USA*. 2005;102:15545–15550.

73. Benjamini Y, Hochberg Y. Controlling the false discovery rate: a practical and powerful approach to multiple testing. *J R Stat Soc B Stat Methodol)*. 2018;57:289–300.

74. Iida M, Fujii S, Uchida M, et al. Identification of aryl hydrocarbon receptor signaling pathways altered in TCDD-treated red seabream embryos by transcriptome analysis. *Aquat Toxicol*. 2016;177:156–170.

75. Storey JD, Tibshirani R. Statistical significance for genomewide studies. *Proc Natl Acad Sci USA*. 2003;100:9440–9445.

76. Jonas JB, Aung T, Bourne RR, Bron AM, Ritch R, Panda-Jonas S. Glaucoma. *Lancet*. 2017;390:2183–2193.

77. Wallace DM, O'Brien CJ. The role of lamina cribrosa cells in optic nerve head fibrosis in glaucoma. *Exp Eye Res*. 2016;142:102–109.

78. Schneider M, Fuchshofer R. The role of astrocytes in optic nerve head fibrosis in glaucoma. *Exp Eye Res*. 2016;142:49–55.

79. Hopkins AA, Murphy R, Irnaten M, Wallace DM, Quill B, O'Brien C. The role of lamina cribrosa tissue stiffness and fibrosis as fundamental biomechanical drivers of pathological glaucoma cupping. *Am J Physiol Cell Physiol*. 2020;319:C611–C623.

80. Kirwan RP, Wordinger RJ, Clark AF, O'Brien CJ. Differential global and extra-cellular matrix focused gene expression patterns between normal and glaucomatous human lamina cribrosa cells. *Mol Vis*. 2009;15:76–88.

81. Hernandez MR, Pena JD. The optic nerve head in glaucomatous optic neuropathy. *Arch Ophthalmol*. 1997;115:389–395.

82. Fukuchi T, Sawaguchi S, Yue BY, Iwata K, Hara H, Kaiya T. Sulfated proteoglycans in the lamina cribrosa of normal monkey eyes and monkey eyes with laser-induced glaucoma. *Exp Eye Res*. 1994;58:231–243.

83. Saini C, Jiang S, Devlin J, et al. Association between HSP-specific T-cell counts and retinal nerve fiber layer thickness in patients with primary open-angle glaucoma. *Ophthalmol Sci*. 2023;3:100310.

84. Ayaki M. Development of neovascular glaucoma in the course of interferon alfa therapy for hepatitis type C. *Br J Ophthalmol*. 1994;78:238.

85. Burgos-Blasco B, Vidal-Villegas B, Saenz-Frances F, et al. Tear and aqueous humour cytokine profile in primary open-angle glaucoma. *Acta Ophthalmol*. 2020;98:e768–e772.

86. Benitez-Del-Castillo J, Cantu-Dibildox J, Sanz-Gonzalez SM, Zanon-Moreno V, Pinazo-Duran MD. Cytokine expression in tears of patients with glaucoma or dry eye disease: a prospective, observational cohort study. *Eur J Ophthalmol*. 2019;29:437–443.

87. Xie RL, Nie HY, Xu YX. Identification of hub genes for glaucoma: a study based on bioinformatics analysis and experimental verification. *Int J Ophthalmol*. 2023;16:1015–1025.

88. Taylor JL, Grossberg SE. The effects of interferon-alpha on the production and action of other cytokines. *Semin Oncol.* 1998;25:23–29.

89. Pinto C, Giordano DM, Maroni L, Marzioni M. Role of inflammation and proinflammatory cytokines in cholangiocyte pathophysiology. *Biochim Biophys Acta Mol Basis Dis.* 2018;1864:1270–1278.

90. Lozano DC, Jayaram H, Cepurna WO, et al. Optic nerve head gene transcription sequelae to a single elevated IOP exposure provides insights into known responses to chronically elevated IOP. *Invest Ophthalmol Vis Sci.* 2023;64:4.

91. Johnson EC, Doser TA, Cepurna WO, et al. Cell proliferation and interleukin-6-type cytokine signaling are implicated by gene expression responses in early optic nerve head injury in rat glaucoma. *Invest Ophthalmol Vis Sci.* 2011;52:504–518.

92. Lozano DC, Choe TE, Cepurna WO, Morrison JC, Johnson EC. Early optic nerve head glial proliferation and Jak-Stat pathway activation in chronic experimental glaucoma. *Invest Ophthalmol Vis Sci.* 2019;60:921–932.

93. Wong M, Huang P, Li W, Li Y, Zhang SS, Zhang C. T-helper1/T-helper2 cytokine imbalance in the iris of patients with glaucoma. *PLoS One.* 2015;10:e0122184.

94. Lachke SA, Alkuraya FS, Kneeland SC, et al. Mutations in the RNA granule component TDRD7 cause cataract and glaucoma. *Science.* 2011;331:1571–1576.

95. Howell GR, Soto I, Zhu X, et al. Radiation treatment inhibits monocyte entry into the optic nerve head and prevents neuronal damage in a mouse model of glaucoma. *J Clin Invest.* 2012;122:1246–1261.

96. Pang IH, Clark AF. Inducible rodent models of glaucoma. *Prog Retin Eye Res.* 2020;75:100799.

97. Emes RD, Goodstadt L, Winter EE, Ponting CP. Comparison of the genomes of human and mouse lays the foundation of genome zoology. *Hum Mol Genet.* 2003;12:701–709.

98. Daniel S, Clark AF, McDowell CM. Subtype-specific response of retinal ganglion cells to optic nerve crush. *Cell Death Discov.* 2018;4:7.

99. Daniel S, Meyer KJ, Clark AF, Anderson MG, McDowell CM. Effect of ocular hypertension on the pattern of retinal ganglion cell subtype loss in a mouse model of early-onset glaucoma. *Exp Eye Res.* 2019;185:107703.

100. Bhattacharyya S, Kelley K, Melichian DS, et al. Toll-like receptor 4 signaling augments transforming growth factor-beta responses: a novel mechanism for maintaining and amplifying fibrosis in scleroderma. *Am J Pathol.* 2013;182:192–205.

101. Guo J, Friedman SL. Toll-like receptor 4 signaling in liver injury and hepatic fibrogenesis. *Fibrogenesis Tissue Repair.* 2010;3:21.

102. Yang L, Seki E. Toll-like receptors in liver fibrosis: cellular crosstalk and mechanisms. *Front Physiol.* 2012;3:138.

103. Seki E, De Minicis S, Osterreicher CH, et al. TLR4 enhances TGF-β signaling and hepatic fibrosis. *Nat Med.* 2007;13:1324–1332.

104. Pulskens WP, Rampanelli E, Teske GJ, et al. TLR4 promotes fibrosis but attenuates tubular damage in progressive renal injury. *J Am Soc Nephrol.* 2010;21:1299–1308.

105. Stoffels JM, Hoekstra D, Franklin RJ, Baron W, Zhao C. The EIIIA domain from astrocyte-derived fibronectin mediates proliferation of oligodendrocyte progenitor cells following CNS demyelination. *Glia.* 2015;63:242–256.

106. Schaefer L, Babelova A, Kiss E, et al. The matrix component biglycan is proinflammatory and signals through Toll-like receptors 4 and 2 in macrophages. *J Clin Invest.* 2005;115:2223–2233.

107. Yanagishita M. Function of proteoglycans in the extracellular matrix. *Acta Pathol Jpn.* 1993;43:283–293.

108. Fukuchi T, Ueda J, Abe H, Sawaguchi S. Cell adhesion glycoproteins in the human lamina cribrosa. *Jpn J Ophthalmol.* 2001;45:363–367.

109. John SW, Smith RS, Savinova OV, et al. Essential iris atrophy, pigment dispersion, and glaucoma in DBA/2J mice. *Invest Ophthalmol Vis Sci.* 1998;39:951–962.

110. Fernandes KA, Harder JM, Williams PA, et al. Using genetic mouse models to gain insight into glaucoma: past results and future possibilities. *Exp Eye Res.* 2015;141:42–56.

111. Chua J, Vania M, Cheung CM, et al. Expression profile of inflammatory cytokines in aqueous from glaucomatous eyes. *Mol Vis.* 2012;18:431–438.

112. Yang X, Zeng Q, Goktas E, et al. T-lymphocyte subset distribution and activity in patients with glaucoma. *Invest Ophthalmol Vis Sci.* 2019;60:877–888.

113. Liu B, Neufeld AH. Expression of nitric oxide synthase-2 (NOS-2) in reactive astrocytes of the human glaucomatous optic nerve head. *Glia.* 2000;30:178–186.

114. Satoh J, Tabunoki H. A comprehensive profile of ChIP-seq-based STAT1 target genes suggests the complexity of STAT1-mediated gene regulatory mechanisms. *Gene Regul Syst Bio.* 2013;7:41–56.

115. Andl CD, Mizushima T, Oyama K, Bowser M, Nakagawa H, Rustgi AK. EGFR-induced cell migration is mediated predominantly by the JAK-STAT pathway in primary esophageal keratinocytes. *Am J Physiol Gastrointest Liver Physiol.* 2004;287:G1227–G1237.

116. Eitsuka T, Tatewaki N, Nishida H, Nakagawa K, Miyazawa T. Synergistic anticancer effect of tocotrienol combined with chemotherapeutic agents or dietary components: a review. *Int J Mol Sci.* 2016;17:1605.

117. Liu B, Neufeld AH. Activation of epidermal growth factor receptor causes astrocytes to form cribriform structures. *Glia.* 2004;46:153–168.

118. Neufeld AH. Nitric oxide: a potential mediator of retinal ganglion cell damage in glaucoma. *Surv Ophthalmol.* 1999;43(suppl 1):S129–S135.

119. Lin CC, Lin WN, Cheng SE, Tung WH, Wang HH, Yang CM. Transactivation of EGFR/PI3K/Akt involved in ATP-induced inflammatory protein expression and cell motility. *J Cell Physiol.* 2012;227:1628–1638.